Nanoscale interfacial defect shedding in a growing nematic droplet

Sebastian Gurevich,[1,2] Nikolas Provatas,[2] and Alejandro Rey[1]
[1]*Department of Chemical Engineering, McGill University, Montreal, QC, Canada*
[2]*Department of Physics, Centre for the Physics of Materials, McGill University, Montreal, QC, Canada*
(Received 31 March 2017; published 11 August 2017)

Interfacial defect shedding is the most recent known mechanism for defect formation in a thermally driven isotropic-to-nematic phase transition. It manifests in nematic-isotropic interfaces going through an anchoring switch. Numerical computations in planar geometry established that a growing nematic droplet can undergo interfacial defect shedding, nucleating interfacial defect structures that shed into the bulk as $+\frac{1}{2}$ point defects. By extending the study of interfacial defect shedding in a growing nematic droplet to larger length and time scales, and to three dimensions, we unveil an oscillatory growth mode involving shape and anchoring transitions that results in a controllable regular distributions of point defects in planar geometry, and complex structures of disclination lines in three dimensions.

DOI: 10.1103/PhysRevE.96.022707

I. INTRODUCTION

Soft matter with orientational ordering is notorious for producing topological defects, which mediate the orientation field and self-assembly of embedded particles. It is responsive to a variety of excitations, making it suitable for a large range of applications. Defect formation is a well-established paradigm for the study of self-organization in material, biological, and astrophysical systems. While the classification and static properties of topological defects have been thoroughly studied [1,2], the exact mechanisms behind their formation and dynamics are relatively unexplored. This is especially remarkable since controlling the orientation field of liquid crystals is the basis of many commercial applications. Polymer-dispersed liquid crystals, which can modulate their opacity in response to an electromagnetic field, are the foundation of current display technologies [3–6]. Liquid-crystal-based sensors exploit the distortions produced in the orientation field in response to interfacial events [7–9]. Orientational ordering is abundant in biological systems. The protein solution that spiders expel to produce silk presents an orientational ordering that is critical to its strength [10]. Structural colors in beetles and flower petals originate in periodic surface nanowrinklings caused by subsurface orientational ordering [11]. Defect formation in liquid crystals plays an important role in testing cosmological models [12–18]. Early universe models postulate a transition from a symmetric phase to a lower-temperature phase where the symmetry is broken. Topological defects formed during the transition act as seeds with extra attractive gravitational force, leading to cosmic structures. In the early universe model of Kibble [19], topological defects such as cosmic strings form at the junctions of uncorrelated growing domains as they merge. The Kibble mechanism was since found to be widespread in both classical and quantum phase transitions.

A liquid crystal undergoing a temperature-driven isotropic-to-nematic phase transition nucleates nematic regions with a length scale in the order of 10 nm [20,21]. The deeper the quench and smaller the seed, the weaker is the anchoring strength at the interface. Small seeds with weak anchoring favor spherically shaped interfaces (circular in two dimensions) since anchoring, the anisotropic contribution to interfacial tension, is negligible [22]. They also favor a uniform orientation field since bulk elasticity dominates over anchoring. Such a seed, in isolation, soon outgrows these nucleation conditions in which anchoring is negligible and grows into an ellipsoid with alternating biaxial and uniaxial interfacial regions corresponding to planar and homeotropic anchoring, respectively. If the growing seed remains isolated, eventually defect structures nucleate on the interface during homeotropic-to-planar or planar-to-homeotropic anchoring transitions. These defect nucleations subsequently shed into the bulk where a well-defined texture stabilizes. The process of interfacial defect nucleation during an anchoring switch and subsequent shedding was introduced by Wincure *et al.* and termed interfacial defect shedding [23–25]. The corresponding numerical simulations in planar geometry established that interfacial defect shedding in a growing nematic droplet leads to the formation of two or four $+\frac{1}{2}$ point defects for shallow or deep quenches, respectively.

For deep quenches, thereafter continues a coexistence of homeotropic and planar anchoring regions at the growing interface, insinuating possible subsequent defect formation events not included in the original Wincure study. We thus extend the numerical study of interfacial defect shedding [23] in a growing nematic droplet to larger length and time scales in planar geometry, and to three-dimensional geometry. We find that within a range of quenches further growth is characterized by an oscillatory growth mode involving shape and anchoring transitions during which defects nucleate at the interface and shed into the bulk. The resulting nematic texture contains a controllable regular distribution of point defects in planar geometry, and complex structures of disclination lines in three dimensions.

II. MODEL AND METHODS

The local orientational ordering can be characterized by the state of the $\mathbf{Q}$ tensor, a symmetric and traceless tensor order parameter that spans an orientation field across the system [1]:

$$\mathbf{Q} = \mu_n \mathbf{nn} + \mu_m \mathbf{mm} + \mu_l \mathbf{ll}, \tag{1}$$

where the orientation is defined with respect to the orthogonal director triad ($\mathbf{n}$,$\mathbf{m}$,$\mathbf{l}$). The isotropic phase corresponds to $\mathbf{Q} = \mathbf{0}$, i.e., three zero eigenvalues $\mu_n = \mu_m = \mu_l = 0$. The nematic uniaxial state corresponds to two equal eigenvalues

and a larger third, whereas a defect is associated with two equal eigenvalues and a smaller third. The nematic biaxial state corresponds to three distinct eigenvalues [26]. The uniaxial and biaxial scalar order parameters S and P quantify the molecular alignment with respect to the main orientation $\mathbf{n}$, which is that of the eigenvector associated to the larger eigenvalue [1]:

$$S = \mathbf{nn}:\mathbf{Q} = \mu_n, \tag{2}$$

$$P = (\mathbf{mm} - \mathbf{ll}):\mathbf{Q} = \mu_m - \mu_l. \tag{3}$$

The uniaxial order parameter $S \in [-0.5,1]$ characterizes the distribution along the main orientation $\mathbf{n}$. Positive values describe prolate distributions, negative values correspond to oblate distributions typical of defects, and $S = 0$ represents isotropic liquid. Prolate and oblate distributions are visualized as prolate and oblate ellipsoids constructed from the tensor $\mathbf{Q} + \mathbf{I}/3$, with $\mathbf{I}/3$ defining a sphere representing isotropic liquid crystal. The biaxial order parameter $P \in [-1.5,1.5]$ characterizes the distribution on the plane normal to the main orientation $\mathbf{n}$. A null value indicates that the projection of the distribution on the plane normal to the main orientation is isotropic, while nonzero values indicate otherwise. In terms of visualization through the $\mathbf{Q} + \mathbf{I}/3$ tensor, a null value indicates the cross section of the ellipsoid is circular, whereas nonzero values indicate it is elliptic with the sign distinguishing the major and minor axis.

On the basis of the classic Landau-de Gennes continuum theory for nematic liquid crystals [1] the total free-energy density f of the nematic-isotropic system can be expressed in terms of the tensor order parameter $\mathbf{Q}$ and its gradients:

$$f = f_h + fg \tag{4}$$

$$f_h(\mathbf{Q}) = \frac{a(T)}{2}\mathbf{Q}:\mathbf{Q} - \frac{b}{3}\mathbf{Q}:(\mathbf{Q}\cdot\mathbf{Q}) + \frac{c}{4}(\mathbf{Q}:\mathbf{Q})^2 \tag{5}$$

$$f_g(\nabla\mathbf{Q}) = \frac{L_1}{2}\nabla\mathbf{Q}\vdots\nabla\mathbf{Q}^t + \frac{L_2}{2}(\nabla\cdot\mathbf{Q})\cdot(\nabla\cdot\mathbf{Q}) + \frac{L_3}{2}\mathbf{Q}:[\nabla\mathbf{Q}:(\nabla\mathbf{Q})^t], \tag{6}$$

where $a(T) = a_0(T - T^*)$, T is the temperature field, and T^* is the clearing point temperature below which the isotropic state is unstable. The material parameters consist of the Landau coefficients a,b,c and the Landau elastic constants L_1,L_2,L_3. The Landau coefficients define the isotropic-nematic transition and the Landau elastic constants couple splay, twist, and bend elastic distortions. The depth of the quench $\Delta T = T^* - T$ controls the isotropic to nematic phase transformation and is only present in the homogeneous energy f_h. The homogeneous energy is invariant under spatial rotations and thus, although sensitive to the magnitude of the orientation field, it is independent of its direction. This rotational invariance can be expressed explicitly in terms of the rotation invariant trace operator, or the uniaxial and biaxial order parameters, by noting that $\mathbf{Q}:\mathbf{Q} = \mathrm{tr}(\mathbf{Q}^2) = \frac{2}{9}(3S^2 + P^2)$ and $\mathbf{Q}:(\mathbf{Q}\cdot\mathbf{Q}) = \mathrm{tr}(\mathbf{Q}^3) = \frac{2}{9}S(S^2 - P^2)$. The orientational elastic energy f_g, however, depends on both the magnitude and the direction of the orientation field.

The Q tensor follows the relaxational dissipative dynamics of model A in the Hohenberg and Halperin classification [27]:

$$\beta\frac{\partial\mathbf{Q}}{\partial t} = -\left(\frac{\partial f}{\partial\mathbf{Q}} + \nabla\cdot\frac{\partial f_g}{\partial\nabla\mathbf{Q}}\right)^{[s]}, \tag{7}$$

where β is a transport coefficient and the superscript $[s]$ denotes symmetric and traceless. Operations on a symmetric traceless tensor do not necessarily produce a symmetric traceless result, hence symmetry and tracelessness are imposed explicitly by replacing each element m_{ij} of the right side tensorial expression with $m_{ij}^{[s]} = (m_{ij} + m_{ji})/2 - \delta_{ij}\mathrm{tr}(M)/3$.

Equation (7) is solved using a finite differences C++ code with OpenMP parallelization developed for both planar and three-dimensional geometry. While the later refers to the dimensionality of the computational domain, in both cases the orientation field is three dimensional. Space is discretized on a simple-square or simple-cubic lattice with mesh size of 1 nm and far-field boundary conditions. In order to minimize the anisotropy created by the grid, a maximally isotropic discretization of gradient operators involving first- and second-neighbor grid points is used. Integration in time uses an explicit Euler scheme. For postprocessing and image generation several PYTHON algorithms were developed. The initial conditions consist of a single spherical (circular on a plane) isolated nematic seed of 2 nm radius with uniform orientation in the x-axis direction, immersed in isotropic liquid of the same material. The system is under a constant and uniform temperature field, i.e., a quench.

The material parameter values correspond to 4′-pentyl-4-cyanobiphenyl, a rodlike thermotropic liquid crystal known as 5CB. Unless otherwise stated, they are given by [24]: $a_0 = 0.14\,\mathrm{MJ/m^3K}$, $T^* = 95.2^\circ\,\mathrm{K}$, $b = 1.8\,\mathrm{MJ/m^3}$, $c = 3.6\,\mathrm{MJ/m^3}$, $L_1 = 3.0\,\mathrm{pJ/m}$, $L_2 = 3.1\,\mathrm{pJ/m}$, $L_3 = 1.5\,\mathrm{pJ/m}$, and $\beta = 0.055\,\mathrm{Js/m^3}$.

III. RESULTS AND DISCUSSION

A nematic seed in isotropic liquid crystal, when under a quench, expands to reduce the overall energy of the system. To do so, it reduces the homogeneous energy at the expense of increasing, at a lower rate, the orientational elastic energy. The orientation field in the growing nematic region hedges the increasing elastic energy by minimizing deviations from the local average orientation in the bulk and from a preferred alignment at the nematic-isotropic interface. The interface alignment is known as anchoring. When $L_2 > 0$ it is preferentially homeotropic, normal to the interface, and when $L_2 < 0$ it is preferentially planar, tangential to the interface [28]. When the contribution of anchoring to interfacial tension is not significant enough, homeotropic and planar anchoring can coexist along different parts of the interface. Transitions between homeotropic and planar anchoring are well described by a double-well anchoring potential. Planar anchoring implies biaxiality at the interface since crossing different phases breaks any nontrivial rotational symmetry on the plane normal to the anchoring orientation. Minimizing deviations from the local average orientation in the nematic bulk is not always compatible with the preferred

alignment at the interface, leading to the emergence of complex textures and the formation of defects.

A. Planar geometry

The early stages of growth under a quench of an initially circular nematic spherulite with uniform orientation were studied in detail by Wincure *et al.* [23–25]. At the onset of growth the spherulite adopts an elliptic shape whose major axis lies along the direction of the initially uniform nematic orientation. This elliptic shape mirrors the Wulff construction or polar plot of the interfacial tension [24], indicating that the anchoring anisotropic contribution to interfacial tension becomes significant once the interface length grows above a threshold. Concurrently, the initially uniform orientation field gives way to a texture dominated by four well-defined interfacial regions centered at the vertices of the ellipse. Two of these are biaxial and correspond to planar anchoring while the other two are uniaxial and correspond to homeotropic anchoring. The latter conserve the nematic orientation of the initial seed. Distinct local curvatures develop in these biaxial and uniaxial regions with a sharp double curvature in between. Subsequently, $+\frac{1}{2}$ defects nucleate at the four interfacial uniaxial-biaxial boundaries for deep quenches, or at the two biaxial vertices for weak quenches. These become point defects as they shed from the interface and migrate into the bulk, forming a well-defined texture of net topological charge $+2$ or $+1$, respectively. The radius of the enclosing circle R, which coincides with the major radius of the ellipse, grows thereafter linearly with time as the interface shape grows more circular, indicating the dominance of a bulk process driven growth indifferent to the (anisotropic) orientation field. This is the texturing process presented by Wincure *et al.* [23–25], displayed in Fig. 1.

Even as the interface shape grows closer to a circle, for deeper quenches ($\Delta T \gtrsim 2$ K) we observe the continuing presence of alternating homeotropic and planar anchoring regions at the interface, as can be seen in Fig. 1(b). This coexistence hints at the possibility of subsequent defect formation events. Indeed, by following further the grow of the nematic spherulite we find that within a range of quench depths early evolution gives way to an oscillatory mode consisting of a series of growth periods mediated by periodic shape and anchoring transitions entailing nucleation of defects. The resulting texture features a regular distribution of point defects along the main axes of growth, i.e., the major and minor axes of the ellipse shaped interface.

During growth periods the major and minor radii of the ellipse shaped interface grow linearly with time. However, the corresponding ratio does not reduce to a constant since both follow a nonhomogeneous linear relation with time. This is because a shape transition precedes each growth period. Thus, during growth periods the elliptic-shaped interface does not scale up as the droplet grows and the ratio of the main radii only tends towards the ratio of their corresponding speeds. The ratio of these speeds is close to unity, making the interface shape evolve towards a circle. The interface shape is thus increasingly altered and the biaxial and uniaxial interfacial regions, which present distinct local curvatures and a sharp double curvature in between, expand. An ensuing localized buildup of interfacial tension eventually triggers a shape transition that removes excess energy into the bulk by means of defect shedding. The latter is characterized by anchoring transitions and four defect nucleations on the vertices of the ellipse, which shed into the bulk as $+\frac{1}{2}$ point defects. The interface adopts a new elliptic shape with the major axis and minor axis switched, and a new growth period ensues. Defect production can thus be viewed as an energy barrier separating local minima of the interfacial energy, a global description of defect production following anchoring transitions that are well described by a double-well anchoring potential. For even deeper quenches, four additional $+\frac{1}{2}$ defects form periodically along the main diagonals of the ellipse. However, the shape transitions are not significantly altered by the corresponding local curvature transformations and the associated local anchoring switch.

The evolution of the total homogeneous energy $F_h = \int f_h d^2x$ and the total elastic energy $F_g = \int f_g d^2x$, for a quench of $\Delta T = 10$ K is shown in Fig. 2. In the inset, a magnified view of the evolution of F_g shows the rise in elastic energy as the spherulite grows. The transfer of energy from the interface to the bulk during shape transitions is negligible

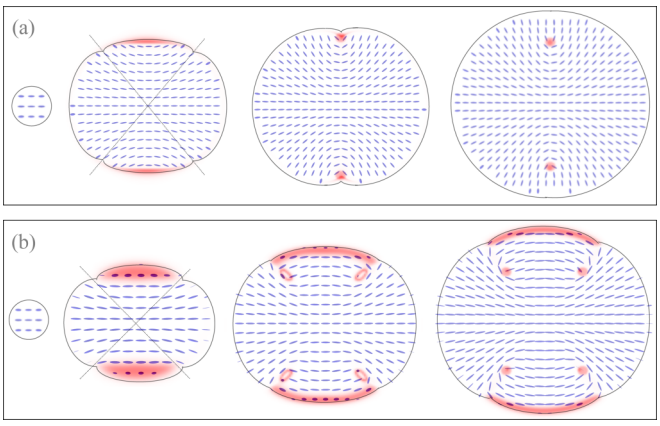

FIG. 1. Early evolution for shallow (a) and deep (b) quenches. Interfacial regions with planar anchoring and defects in the bulk, both highly biaxial, are highlighted. Not to scale.

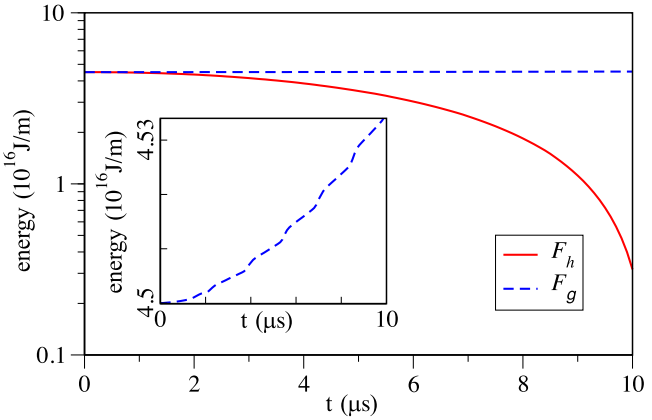

FIG. 2. Total homogeneous and elastic energies, $F_h = \int f_h d^2x$ and $F_g = \int f_g d^2x$, for a quench of $\Delta T = 10$ K. The inset shows a magnified view of F_g.

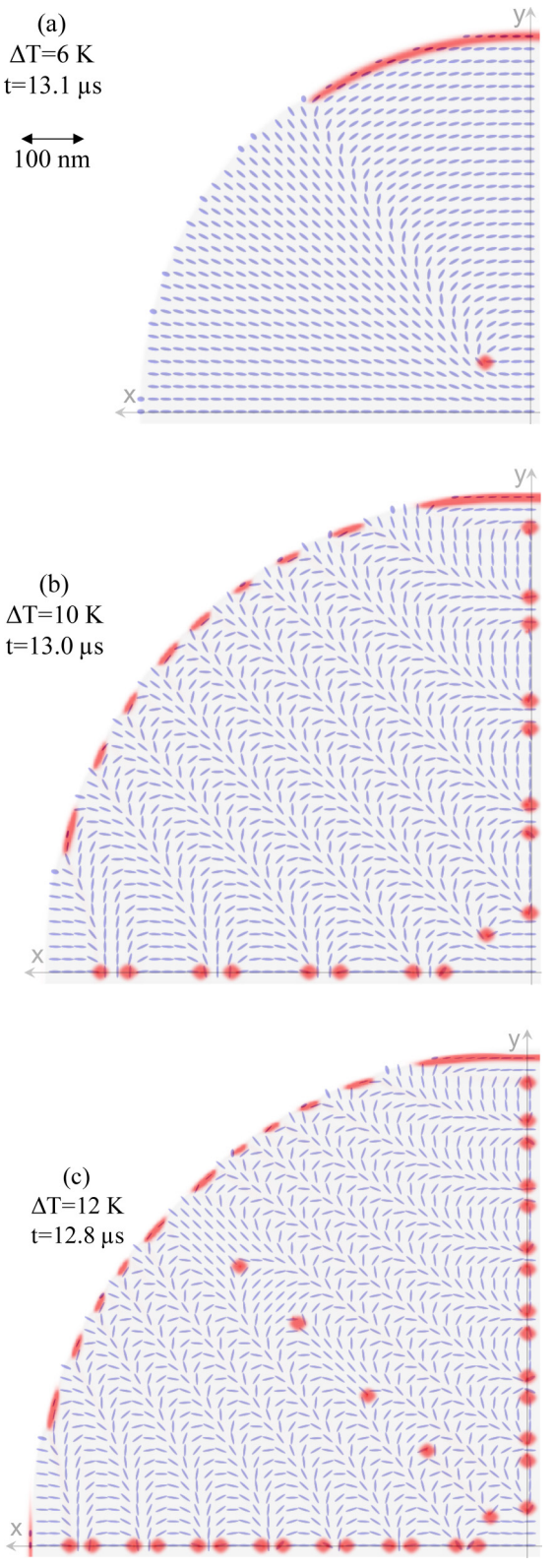

FIG. 3. Orientation field and defects distribution. Interfacial regions with planar anchoring and defects, both highly biaxial, are highlighted. For visualization, and given its fourfold symmetry, about a quarter of the droplet is shown. The shaded region is where $S > 0$, marking the extent of the nematic droplet.

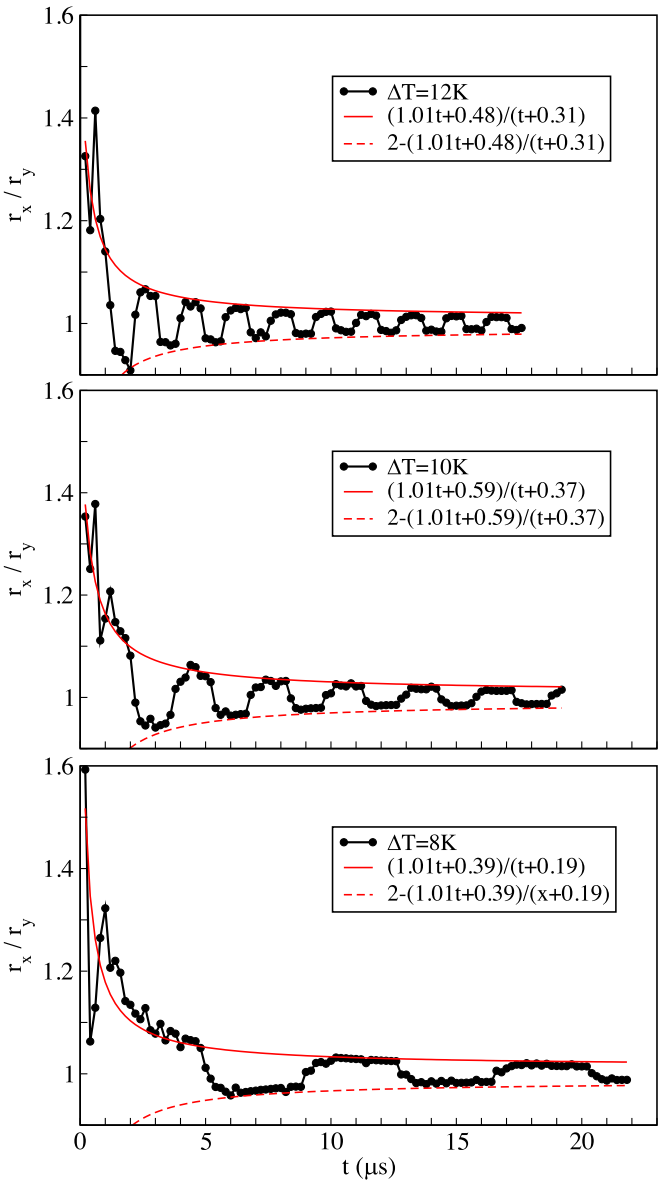

FIG. 4. Evolution of the main radii ratio for different quenches. Guidelines are included.

in the scale of the main plot. However, its effect on the rate of increase of the total elastic energy creates the oscillations visible in the inset plot.

For weak quenches ($\Delta T \lesssim 2$ K) only the original Wincure texturing process develops after which the whole nematic-isotropic interface is uniaxial, as shown in Fig. 1(a). The absence of biaxial regions along the interface implies no further defect formation events are expected. For intermediate quenches ($2\ \text{K} \lesssim \Delta T \lesssim 10\ \text{K}$) the resulting texture features uniformly distributed pairs of defects along the main axes, and for deeper quenches additional pairs of defects form along the main diagonals, as shown in Fig. 3.

The evolution of the interface shape can be characterized by tracing the ratio of the main radii. Typical examples for different quench depths are shown in Fig. 4, where the x

axis coincides with the uniform orientation field in the initial nematic seed. Results for early times naturally present a larger spread as both numerator and denominator are small. We include guidelines whose functional form derives from assuming that during growth periods the radii grow linearly with time. These guidelines are formally defined as $\frac{r_x}{r_y} = \frac{v_x t + r_{x0}}{v_y t + r_{y0}}$ where v_x and v_y are the local velocity of the vertices while r_{x0} and r_{y0} are the respective radii intercepts. Given the ambiguity in this expression, as only three of the four parameters are independent, we normalize it by dividing both numerator and denominator by v_y. We also include the mirror image of the guidelines with respect to $\frac{r_x}{r_y} = 1$ to emphasize the symmetry. Note that since every linear growth regime follows a shape transition, we cannot assume the radii intercepts are equal to the radius of the initial droplet $r_{\nu 0} \neq r_\nu(t=0), \nu = x, y$. A stricter analysis would require fitting each growth period separately, with each linear fitting having its own intercepts. However, our approach is qualitative. Since shape transitions are short lived, we find it is illuminating to fit the whole time range. This approach highlights that even though shape transitions switch the major and minor axis, they do not alter the overall evolution of the major to minor radius ratio.

The long-term limit of the radii ratio is the ratio of their speeds $\frac{v_x}{v_y}$. We find it is close to unity, which is consistent with growth being dominated by (minimization of) the homogeneous energy as it is independent of the direction of the nematic orientation field. The ratio of the speeds shows only a small increase with the quench depth ΔT, of the order of the thousandths. An increase is consistent with growth being driven by (minimization of) the homogeneous energy, but its small magnitude is somewhat surprising. It is possible that in determining the interface speed the term carrying the temperature dependence is the least dominant in Eq. (5). Contrastingly, the ratio $\frac{r_{x0}}{r_{y0}}$ decreases with the quench depth ΔT as the influence of the orientation field on shape selection during the onset of growth, and during shape transitions, decreases. During growth periods the speed of each main radii remains constant, and during shape transitions they switch. The interface shape oscillates between two increasingly circular ellipses rather than approach continuously a circular shape. We estimate that if the spherulite were to keep growing indefinitely even intermediate quenches may eventually lead to the formation of pairs of defects along the main diagonals. Ultimately, defects might even form along other diagonals as the interface keeps expanding. The damping of the shape oscillations, i.e., the interface becoming increasingly circular, may call into question the long-term continuity of defect production in the growing nematic spherulite. However, the continued coexistence of biaxial and uniaxial regions at the interface, the presence of distinct local curvatures, the localized nature of defect formation and the fact that the ratio of the main radii speeds, although close to unity, is not precisely one suggests that the spherulite never reaches a perfectly circular shape and defect production can possibly continue indefinitely, likely complemented by defect production along diagonals to the main axes.

Defects nucleate periodically along the main axes during shape transitions. As a defect sheds into the bulk its position is adjusted by the relaxation of the orientational elastic energy.

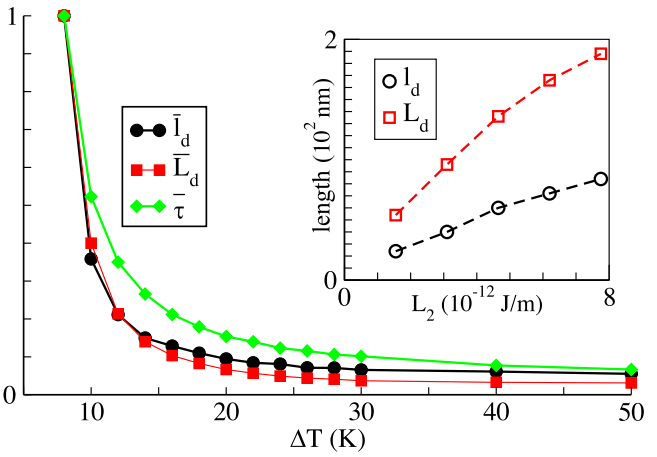

FIG. 5. Normalized defect distances along the main axes $\bar{L}_d = \frac{L_d}{240nm}$, $\bar{l}_d = \frac{l_d}{111nm}$, and normalized periodicity of shape transitions $\bar{\tau} = \frac{1.2\tau}{\mu s}$, as functions of quench depth ΔT. In the inset, L_d and l_d dependence with L_2 for $\Delta T = 10$ K.

Consequently, the resulting distribution of defects along the main axes does not fully correlate with the interface shape evolution history. This distribution consists of uniformly spaced pairs of defects, with the distance between neighboring defects alternating between L_d and $l_d < L_d$. Both distances decrease with the depth of the quench and can be scaled to a single curve as shown in Fig. 5. The normalized periodicity of shape transitions $\bar{\tau} = \frac{1.2\tau}{\mu s}$ consistently does not scale with the distances between defects. The scaling of L_d and l_d can be formalized as $\frac{L_d}{l_d} = \epsilon_d \ell_d(\Delta T)$, where $\ell_d(\Delta T)$ carries the dependence with the depth of the quench and ϵ_d depends on the material parameters. For a given set of material parameters, the depth of the quench controls the location of defect formation but not the further adjustment due to the relaxation of the orientational elastic energy during defect shedding. It is tempting to assume that ϵ_d depends solely on the Landau elastic constants L_1, L_2, L_3 of Eq. (6) and that $\ell_d(\Delta T)$ solely depends on the Landau coefficients $a_0 \Delta T, b, c$ defining the isotropic-nematic transition in Eq. (5). However, while ϵ_d does seem to depend solely on the Landau elastic constants, these also affect the frequency and location of defect formation, indicating that $\ell_d(\Delta T)$ depends on all the material parameters. The dependence of L_d and l_d with the Landau elastic constant L_2 for a quench of $\Delta T = 10^\circ$ K is shown in the inset of Fig. 5. Both L_d and l_d, as their difference, increase with L_2. Increasing L_2 rises the orientational elasticity strength, surface tension, and the time period between shape transitions, leading to larger L_d and l_d. Increasing the orientational elasticity strength also intensifies the energy cost of deviations from the local average orientation in the nematic bulk, affecting the defect positional adjustment during defect shedding as it follows the development of the orientation field in the growing nematic bulk. Given that the curves of L_d and l_d in Fig. 5 scale, it is possible to speculate that the dependence on the Landau coefficients follows an inverse power law and the dependence on the Landau elastic constants follows a power law. The dimensions of the Landau coefficients J/m^3 and the Landau elastic constants J/m further suggest that they may be coupled through a characteristic length squared, or the product of two characteristic lengths.

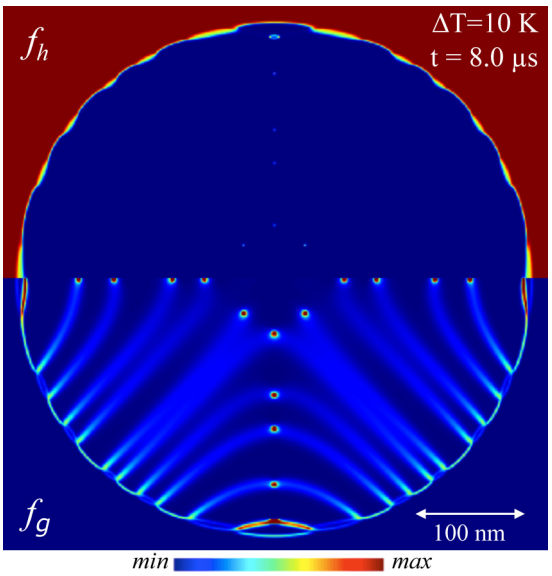

FIG. 6. Homogeneous (f_h) and elastic (f_g) energies in planar geometry.

It is noteworthy that the formation of defects along the diagonals for larger quenches has no bearings on the dynamics and dependences of defect formation along the main axes, consistently with defect formation being a local process.

The nematic bulk is characterized by domains with distinct texture separated by high elastic-energy boundary walls that are precursors to defect formation, and thus contain the defects. Boundary walls are biaxial ($|P| > 0$), although not as intensely as defects and interfacial regions with planar anchoring. Figure 6 displays the homogeneous and elastic energies for a spherulite growing under a $\Delta T = 10$ K quench. Along the nematic-isotropic interface the biaxial regions present higher elastic energy than the uniaxial regions, in accordance with anchoring being preferentially normal to the interface (homeotropic). Interestingly, the local maximum of the homogeneous energy in the uniaxial interfacial regions spreads to fill the local concavities. The density of boundary walls, their curvature and their length correlates to the distribution and amount of defects. The innermost boundary walls pass through the first defects formed during the initial texturing process described by Wincure *et al.* The relative position of these Wincure defects can be estimated by minimizing the total energy (bulk elasticity, surface tension, and boundary walls) with respect to the curvature or aperture angle, as was done in Ref. [29]. Estimating the positions of the defects along the main axes can in principle be accomplished in the same manner, but involves more complex geometries. For our purposes it is enough to note that increasing the elastic energy amplifies the defects positional adjustment during shedding, magnifying the difference between l_d and L_d, while the position at which defects form can be controlled by the depth of the quench as noted above, or by manipulating the anchoring strength. Magnifying the anchoring strength increments the time period between shape transitions and therefor increases both L_d and l_d. It would thus be straightforward to tune the positions of the defects by modifying the depth of the quench, anchoring or the orientational elasticity strength. A systematic study of the effects of these modifications may even allow us to extract phenomenologically functional dependencies for the defect positions.

B. Three-dimensional geometry

Free boundary problems present an enormous reduction in computational efficiency when increasing dimensionality since processing and memory requirements normally scale with domain size. Many numerical and computational approaches have been devised to mitigate this efficiency loss. Among the most common are lowering the effective dimensionality through restricting to specific symmetries, employing passive or active adaptive meshes with increased resolution around phase boundaries and parallelization through multiprocessing, multithreading, and graphic processing units. While forcing a symmetry can only uncover solutions compatible with that symmetry, adaptive-mesh techniques become superfluous when bulks and phase boundaries require comparable mesh resolutions. Our three-dimensional simulations are performed on a uniform mesh, employ multithreading parallelization and use the same initial, run-time and far-field boundary conditions as those in planar geometry.

The initial conditions correspond to a spherical nematic seed immersed in isotropic liquid crystal of the same material. The uniform orientation field within the seed, along the x axis, breaks the otherwise highly spherical symmetry of the system. Along the spherical surface of the initial nematic seed the orientation field varies continuously between perpendicular and tangential. As the seed starts expanding the anchoring elastic energy will drive the orientation field at the interface to perpendicular (preferentially) or tangential, while bulk elasticity will resist local orientation distortions. The growth of the nematic phase is dominated by the minimization of the homogeneous energy. Interface morphology and texturing within the droplet are governed by the competition between bulk and interface orientational elasticity. The dynamics mirrors that in planar geometry but the resulting texture is topologically more complex. In three dimensions disclination lines can be energetically favorable over point defects and are able to stabilize through geometric or intrinsic constraints [30–32]. The closed nematic-isotropic interface screens external effects and allows only closed defect loops or disclinations that close to the interface. The lack of obstructions leads to highly symmetric structures. These conditions favor the formation of knotted defect structures, especially since knotting is topologically stabilizing.

At the onset of growth, as the anisotropic contribution of anchoring to the total interfacial tension becomes significant, the initially spherical seed grows into an ellipsoid whose major axis lies along the direction of the initially uniform orientation field, i.e., the x axis. Concurrently the orientation field becomes axisymmetric with respect to the x axis, presenting a longitudinal cross section that closely resembles the texture of the equivalent stage of growth in planar geometry shown in Fig. 1(b). On the ellipsoid-shaped nematic-isotropic interface, the orientation field distinguishes three distinct simply connected surfaces. A biaxial barrel-shaped surface revolving around the x axis with corresponding planar anchoring, and two uniaxial curved surfaces at opposing poles on the x axis

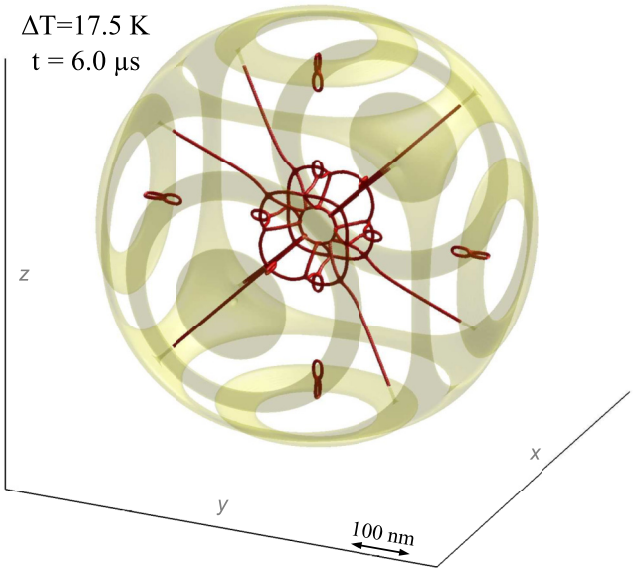

FIG. 7. Highly biaxial regions ($|P| > 1.2$), distinguishing interface from bulk.

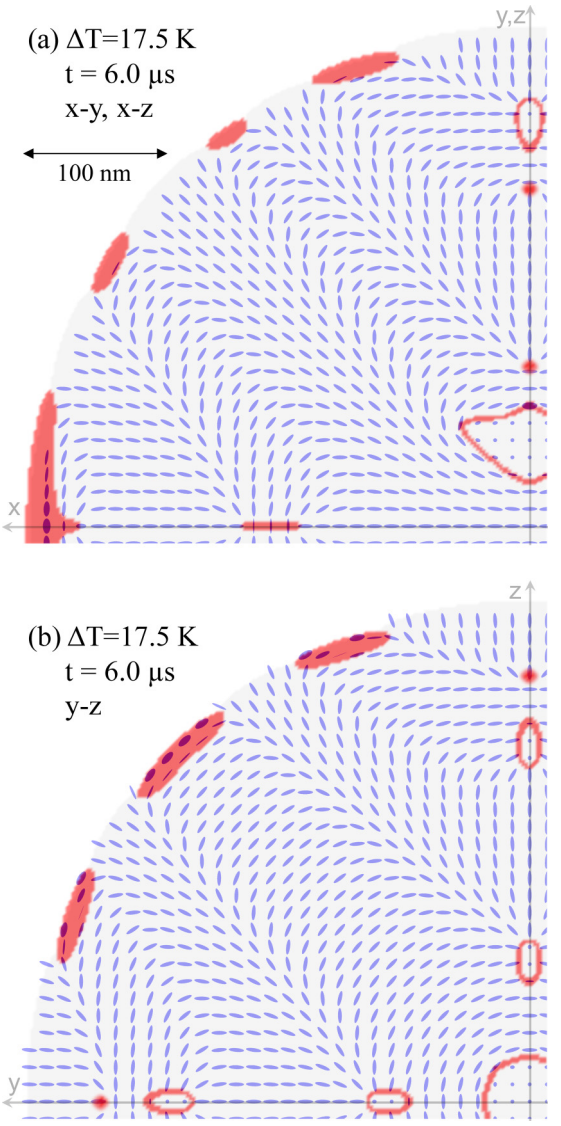

FIG. 8. Orientation field and distribution of defects in three-dimensional geometry, projected on different planes. Interfacial regions with planar anchoring and defects, both highly biaxial, are highlighted. For visualization, and given its fourfold symmetry, about a quarter of the projection is shown. The shaded region is where $S > 0$, marking the extent of the nematic droplet. The projections on the xy and xz planes are identical.

with corresponding homeotropic anchoring. The latter largely preserve the texture of the initial seed. Distinct local curvatures develop in the biaxial and uniaxial interfacial regions with a double curvature in between. As the seed grows further the double-curvature region may destabilize and form disclination lines that shed into the bulk. Like in planar geometry, within a range of quench depths early evolution is followed by an oscillatory growth mode with a series of periodic shape and anchoring transitions entailing nucleation of defect structures. The interface shape alternates between increasingly spherical prolate and oblate ellipsoids and each defect nucleation on the two main axes perpendicular to the x axis stabilize into a twisted-double-torus disclination line knot as it sheds into the bulk. Each twisted-double-torus disclination line knot cannot collapse into a point defect, nor dissipate. As growth proceeds, the twisted-double-torus disclination line knots organize in a regular distribution along the axes where they are formed. The lack of charge conservation is consistent with an orientation far field that is not uniform nor constant.

Size limitations on the computational domain prevent us from confirming the pairs distribution we observe in planar geometry. The similarities in evolution and texture allow assessing that the ensembles of twisted-double-torus disclination line knots will organize similarly to the equivalent ensemble of point defects in planar geometry. It is yet to be determined, however, if each disclination line knot will assume the role taken in planar geometry by a single defect point, or by a pair of point defects. We expect the distances between the twisted-double-torus disclination line knots to differ from the distances between point defects (l_d), or pairs of point defects (L_d), in the equivalent stage of growth in planar geometry. Especially given that, when compared to planar geometry, the high elastic energy domain walls in the nematic bulk have an extra dimension to fold in. We do expect the same tendencies when varying the material and control parameters. As in planar geometry, increasing the elastic energy amplifies the defects positional adjustment during shedding while the periodicity of the shape transitions follows the depth of the quench and the anchoring strength. The twisted-double-torus disclination line knots can be seen in the example presented in Fig. 7.

The projections of the orientation field on the main planes are reminiscent of the orientation field in planar geometry at the same stage of growth, as can be seen in Fig. 8. Figure 9 displays the homogeneous (f_h) and elastic (f_g) energies for the same instance shown in Figs. 7 and 8. These highlight that the nematic bulk is characterized by nematic volumes with distinct texture whose boundaries are high elastic-energy two-dimensional walls. The boundary walls are precursors to defect formation, and thus contain the defects. Their density and morphology correlates with the amount and morphology

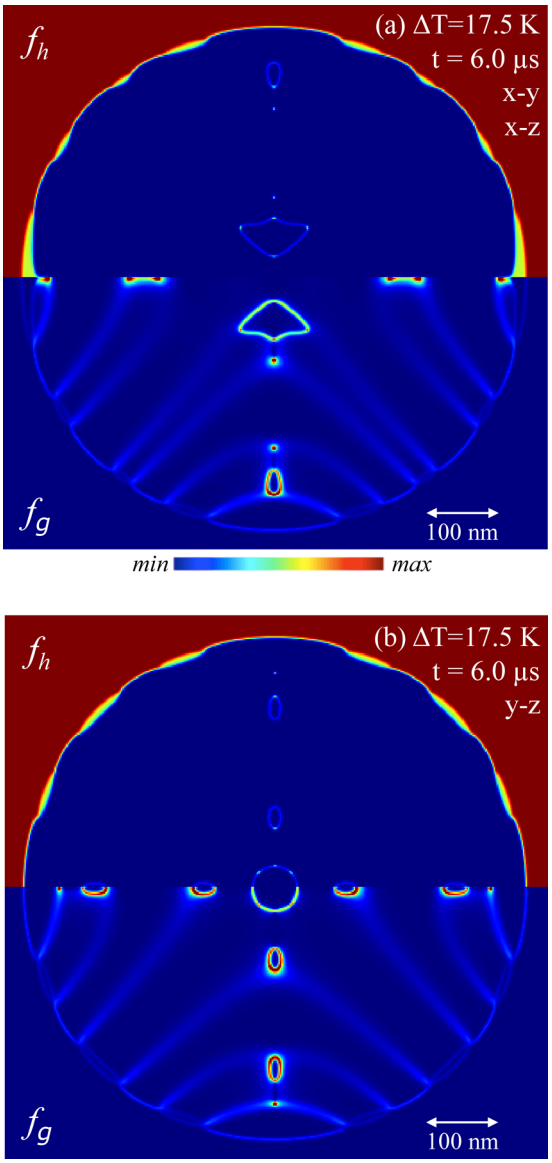

FIG. 9. Homogeneous (f_h) and elastic (f_g) energies in three-dimensional geometry, projected on the xy plane (top) and the yz plane (bottom). The projections on the xy and xz planes are identical.

of the defects structures. Disclinations align with their planes perpendicular to the orientation field to minimize elastic distortions. The innermost boundary walls pass through the defect structure formed during the initial texturing process. In planar geometry deep quenches produce four point defects at the center of the droplet. In three-dimensional geometry they produce at the core of the droplet an entangled disclination loop that may be of complex geometry, and can comprise disclinations of lower and higher strengths that locally obey the Kirchhoff topological conservation law at the junctions [33,34]. This defect structure at the core is either freestanding or, for deeper quenches, connects to the nematic-isotropic interface along the main diagonals of the ellipsoid shaped droplet. The limiting quench depth is similar to that at which in planar geometry additional pairs of defects form along the diagonals ($\Delta T \sim 12$ K), hinting at a connection.

Knotted disclination lines in liquid crystals are attracting much attention as means to study knotted configurations, driven by the development of innovative experimental techniques to form and manipulate knotted defect structures [35–40]. Knots of disclination lines in liquid crystals have been observed only in chiral, symmetry-breaking systems. Their formation in nematic liquid crystal droplets, under highly symmetric confinement, may seem surprising since it is not the media but the initial state of the orientation field that provides a privileged direction that breaks the spherical symmetry. The long-term stability of these knotted defect structures is as important when considering whether experimental observations are possible. In particular, disclination line knots are yet to be observed experimentally even in chiral nematic droplets. A more detailed analysis of the entangled defect loop at the core of the droplet as part of the emerging research on knotted fields is a subject for future research.

IV. CONCLUSIONS

Extending the study of interfacial defect shedding in a growing nematic droplet reveals that this setting can produce a controllable regular distributions of point defects in planar geometry and complex structures of disclination lines in three dimensions. Moreover, it reveals that interfacial defect shedding is not only intimately associated with local interfacial shape changes, but also with global interfacial variations.

Experimental observation of interfacial defect shedding in a growing nematic droplet is an ongoing challenge given the short time and small length scales involved. Numerical predictions not only expand our knowledge and inspire experimental methods, they play an important role in interpreting nanoscale experimental results. The optical methods commonly used to observe liquid crystal droplets have a resolution that is limited to the micrometer scale [21,41,42]. Other techniques such as deuterium magnetic resonance (^{2}H-NMR) can be used successfully in smaller length scales [41,43,44]. However, the experimental ^{2}H-NMR spectrum needs to be compared to a simulated spectral pattern of the predicted texture in order to interpret the results [41]. Other visualization techniques capable of capturing the Kibble mechanism at small length scales may be worth exploring in pursuit of observing interfacial defect shedding, even if not in the context of an isolated growing nematic droplet in the absence of external fields. Bose-Einstein condensation in trapped cold gases [45,46], vortices in multiferroic hexagonal manganites heated above the ferroelectric transition temperature [47], ion Coulomb crystals [48], and two-dimensional ensembles of colloidal particles [49] have all proven suitable for observing experimentally the Kibble mechanism. Further opportunities may reside in manipulating boundary conditions [50] and externally controlled fields [51]. State-of-the-art high-speed optical imaging such as ultrafast optical shutters in combination with femtosecond laser pulses may eventually be able to capture interfacial defect shedding in a growing isolated nematic droplet. However, this would require careful consideration of the morphological responses following the pulse irradiation.

Certain experimental validation can be found, nevertheless. Observations of nematic 5CB in cylindrical cavities surface treated with lecithin, which favors homeotropic anchoring

and weakens the anchoring strength, show that the resulting equilibrium nematic texture is very similar to the texture predicted immediately before interfacial defect shedding [41]. Oscillatory modes between defect configurations have been recently reported in active nematic vesicles [52] and active nematic shells [53]. Even though the geometry and driving mechanisms are different, they demonstrate oscillatory responses of a nematic liquid crystal under topological constraints. The potential of the (orientational) elastic energy to generate oscillatory dynamics is often obscured by the homogeneous energy dominating the isotropic-to-nematic phase transformation. It is thus not trivial to discover conditions for which an oscillatory response arises.

Interfacial defect shedding can coexist with the Kibble mechanism, which was first proposed in the context of cosmology as responsible for the creation of domain structures during the early universe expansion, modeled as a temperature-induced phase transition. Combining both defect forming mechanisms, or exploring interfacial defect shedding alone, as an alternative mechanism for symmetry breaking in early universe models may be of particular interest in cosmology. For favoring the formation of knotted defect structures in three dimensions, interfacial defect shedding in a growing nematic droplet can also play an important role in the emerging research on knotted fields, where entangled defect line knots in liquid crystals are becoming a paradigm for studying knotted configurations.

Our results highlight how the nonequilibrium dynamics of active matter can be exploited to produce defect configurations in a controlled manner. Expanding our knowledge of the physics of liquid crystals has much potential in developing functional materials for multiple applications as well as in building theoretical models for material, biological, and astrophysical systems.

ACKNOWLEDGMENT

This work was supported by the Natural Science and Engineering Research Council of Canada (NSERC). We thank Compute Canada for computing resources.

[1] P. G. de Gennes, *The Physics of Liquid Crystals*, 2nd ed. (Clarendon Press, New York, 1993).
[2] N. D. Mermin, Rev. Mod. Phys. **51**, 591 (1979).
[3] J. W. Doane, N. A. Vaz, B.-G. Wu, and S. Žumer, Appl. Phys. Lett. **48**, 269 (1986).
[4] P. S. Drzaic, J. Appl. Phys. **60**, 2142 (1986).
[5] R. B. Meyer, Phys. Rev. Lett. **22**, 918 (1969).
[6] H. G. Craighead, J. Cheng, and S. Hackwood, Appl. Phys. Lett. **40**, 22 (1982).
[7] E. Tjipto, K. D. Cadwell, J. F. Quinn, A. P. R. Johnston, N. L. Abbott, and F. Caruso, Nano Lett. **6**, 2243 (2006).
[8] V. K. Gupta, J. J. Skaife, T. B. Dubrovsky, and N. L. Abbott, Science **279**, 2077 (1998).
[9] Y.-Y. Luk, M. L. Tingey, D. J. Hall, B. A. Israel, C. J. Murphy, P. J. Bertics, and N. L. Abbott, Langmuir **19**, 1671 (2003).
[10] A. D. Rey and E. E. Herrera-Valencia, Biopolymers **97**, 374 (2012).
[11] P. Rofouie, D. Pasini, and A. D. Rey, J. Chem. Phys. **143**, 114701 (2015).
[12] M. J. Bowick, L. Chandar, E. A. Schiff, and A. M. Srivastava, Science **263**, 943 (1994).
[13] W. Zurek, Phys. Rep. **276**, 177 (1996).
[14] T. W. B. Kibble, Aust. J. Phys. **50**, 697 (1997).
[15] H.-R. Trebin, Liq. Cryst. **24**, 127 (1998).
[16] A. M. Srivastava, Pramana **53**, 1069 (1999).
[17] A. Rajantie, Int. J. Mod. Phys. A **17**, 1 (2002).
[18] M. Simoes and M. Pazetti, Europhys. Lett. **92**, 14001 (2010).
[19] T. W. B. Kibble, J. Phys. A: Math. Gen. **9**, 1387 (1976).
[20] O. Lavrentovich, in *Patterns of Symmetry Breaking*, edited by H. Arodz, J. Dziarmaga, and W. Zurek, NATO Science Series (Springer, Netherlands, 2003), Vol. 127, pp. 161–195.
[21] S. Bronnikov and I. Dierking, Phys. Chem. Chem. Phys. **6**, 1745 (2004).
[22] A. K. Bhattacharjee, Sci. Rep. **7**, 40059 (2017).
[23] B. M. Wincure and A. D. Rey, Nano Lett. **7**, 1474 (2007).
[24] B. M. Wincure, Ph.D. thesis, National Library Collection Copies: NL Stacks - Mic.F. TK- 38662, McGill University, 2007.
[25] B. Wincure and A. D. Rey, J. Chem. Phys. **124**, 244902 (2006).
[26] A. D. Rey, Macromol. Theory Simul. **4**, 857 (1995).
[27] P. C. Hohenberg and B. I. Halperin, Rev. Mod. Phys. **49**, 435 (1977).
[28] P. J. Collings and J. S. Patel, *Handbook of Liquid Crystal Research* (Oxford University Press, New York, 1997).
[29] S. Gurevich, E. Soule, A. Rey, L. Reven, and N. Provatas, Phys. Rev. E **90**, 020501 (2014).
[30] Y. Hu, Y. Qu, and P. Zhang, Commun. Comput. Phys. **19**, 354 (2016).
[31] S. Mkaddem and E. C. Gartland, Phys. Rev. E **62**, 6694 (2000).
[32] E. C. Gartland and S. Mkaddem, Phys. Rev. E **59**, 563 (1999).
[33] A. Shams, X. Yao, J. O. Park, M. Srinivasarao, and A. D. Rey, Soft Matter **8**, 11135 (2012).
[34] M. Kleman and C. Williams, Philos. Mag. **28**, 725 (1973).
[35] U. Tkalec, M. Ravnik, S. Čopar, S. Žumer, and I. Muševič, Science **333**, 62 (2011).
[36] E. Terentjev, Nat. Mater. **12**, 187 (2013).
[37] T. Machon and G. P. Alexander, Phys. Rev. Lett. **113**, 027801 (2014).
[38] D. Sec, S. Copar, and S. Zumer, Nat. Commun. **5**, 3057 (2014).
[39] A. Martinez, M. Ravnik, B. Lucero, R. Visvanathan, S. Zumer, and I. I. Smalyukh, Nat. Mater. **13**, 258 (2014).
[40] S. Copar, U. Tkalec, I. Musevic, and S. Zumer, Proc. Natl. Acad. Sci. USA **112**, 1675 (2015).
[41] G. P. Crawford, D. W. Allender, and J. W. Doane, Phys. Rev. A **45**, 8693 (1992).
[42] S. Bronnikov and I. Dierking, Physica B **358**, 339 (2005).
[43] J. H. Erdmann, S. Žumer, and J. W. Doane, Phys. Rev. Lett. **64**, 1907 (1990).
[44] G. P. Crawford, M. Vilfan, J. W. Doane, and I. Vilfan, Phys. Rev. A **43**, 835 (1991).

[45] G. Lamporesi, S. Donadello, S. Serafini, F. Dalfovo, and G. Ferrari, Nat. Phys. **9**, 656 (2013).
[46] J. Beugnon and N. Navon, J. Phys. B: At. Mol. Opt. Phys. **50**, 022002 (2017).
[47] S.-Z. Lin, X. Wang, Y. Kamiya, G.-W. Chern, F. Fan, D. Fan, B. Casas, Y. Liu, V. Kiryukhin, W. H. Zurek, C. D. Batista, and S.-W. Cheong, Nat. Phys. **10**, 970 (2014).
[48] K. Pyka, J. Keller, H. L. Partner, R. Nigmatullin, T. Burgermeister, D. M. Meier, K. Kuhlmann, A. Retzker, M. B. Plenio, W. H. Zurek, A. del Campo, and T. E. Mehlstäubler, Nat. Commun. **4**, 2291 (2013).
[49] S. Deutschlander, P. Dillmann, G. Maret, and P. Keim, Proc. Natl. Acad. Sci. USA **112**, 6925 (2015).
[50] M. Nikkhou, M. Škarabot, S. Čopar, and I. Muševič, Eur. Phys. J. E **39**, 100 (2016).
[51] M. Nikkhou, M. Skarabot, S. Copar, M. Ravnik, S. Zumer, and I. Musevic, Nat. Phys. **11**, 183 (2015).
[52] F. C. Keber, E. Loiseau, T. Sanchez, S. J. DeCamp, L. Giomi, M. J. Bowick, M. C. Marchetti, Z. Dogic, and A. R. Bausch, Science **345**, 1135 (2014).
[53] R. Zhang, Y. Zhou, M. Rahimi, and J. J. de Pablo, Nat. Commun. **7**, 13483 (2016).